

Supplementary Information for:
Fullerene Embedded Shape Memory Nanolens Array

So Hee Jeon^{1#}, Jun Young Jang^{2#}, Jae Ryoun Youn^{1#}, Jun-ho Jeong³, Howard Brenner⁴, Young Seok Song^{2*}

¹Research Institute of Advanced Materials (RIAM),
Department of Materials Science and Engineering, Seoul National University,
Daehak-Dong, Gwanak-Gu, Seoul 151-744, Korea

²Department of Fiber System Engineering, Dankook University,
126 Jukjeon-dong, Suji-gu, Yongin-si, Gyeonggi-do 448-701, Korea

³Nano-Mechanical Systems Research Center, Intelligent and Precision Machinery Research Division,
Korea Institute of Machinery and Materials, 104 Sinseongno, Yuseong-gu, Daejeon, 305-343,
Republic of Korea

⁴Department of Chemical Engineering, Massachusetts Institute of Technology, Cambridge,
Massachusetts 02139, USA

*Corresponding author: Young Seok Song

Tel.: +82-31-8005-3567; Fax: +82-31-8005-2209; E-mail: ysong@dankook.ac.kr

#These authors contributed equally to this paper

The supplementary contains more information on:

- 1. Constitutive modeling**
- 2. Materials**
- 3. Preparation methods**
- 4. Morphological analysis**
- 5. Optical analysis**
- 6. Mechanical analysis**
- 7. Contact angle analysis**
- 8. Supplementary references**

1. Constitutive modeling

Constitutive modeling explaining the relationship between applied stress and strain allows us to understand the thermophysical behavior of materials in a more theoretical manner. The numerical modeling employed in this study is based on the literature ^{21, 31, 32}. The modeling includes the following four stages: (i) loading (deformation), (ii) cooling, (iii) unloading, and (iv) heating (recovery). The stress-strain-temperature diagram showing the thermomechanical behavior of a shape memory polymer (SMP) is presented in Fig. S1 ^{33, 34}. The thermomechanical cycle begins from a high temperature, point (I), where SMPs experience a mechanical loading and are deformed to point (II). At this point, a constant strain is maintained, and temperature decreases down to point (III). During this process, the rubbery state of SMPs changes to the glassy state. An SMP shows both the rubbery and glassy behaviors around the glass transition temperature. At point (III), the unloading process starts. Since the glassy phase has much higher stiffness than the rubbery phase, the resulting strain changes slightly toward point (IV). Lastly, the temperature increases by means of the microwave irradiation, which leads to the shape recovery of SMPs. This cycle is referred to as a stress-free strain recovery of SMPs. The relevant governing equations for the constitutive modeling are presented in the next sections.

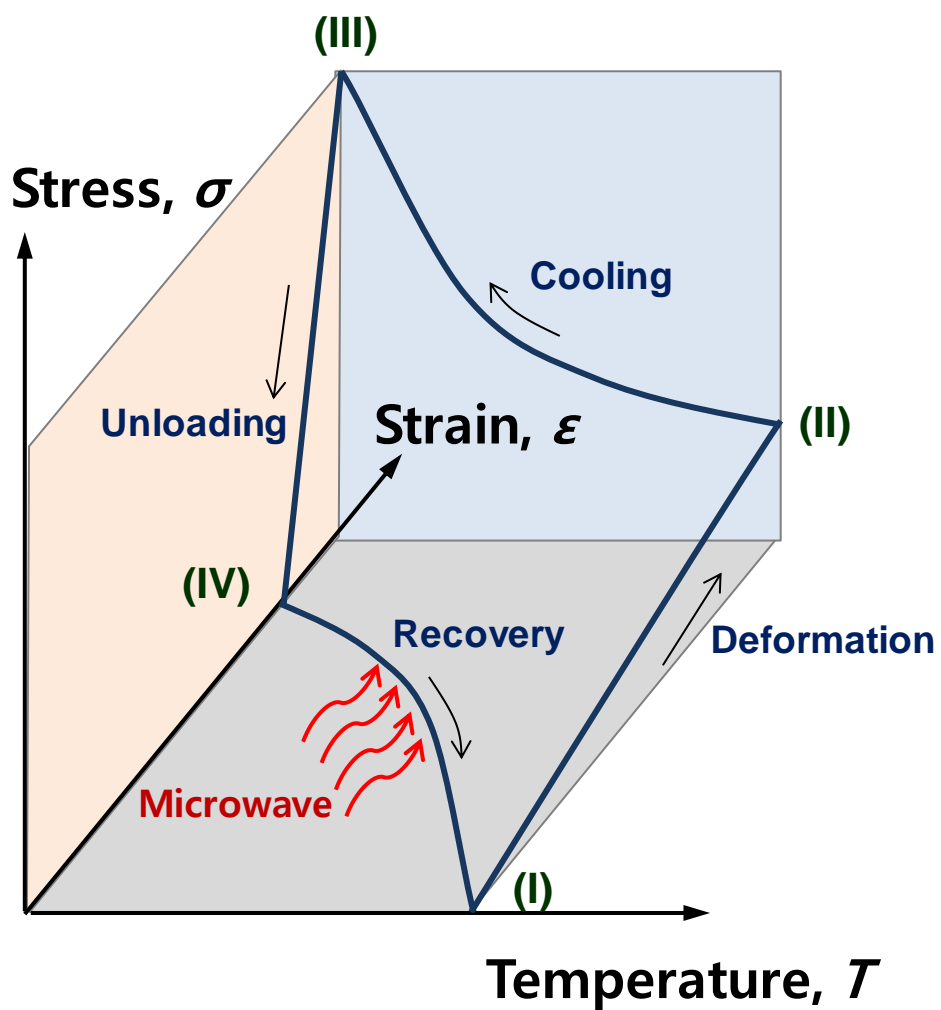


Fig. S1. Stress-strain-temperature diagram. This diagram demonstrates the thermomechanical behavior of SMPs under stress-free constrain condition. The cycle encompasses deformation, cooling, unloading, and recovery. In particular, the recovery (heating) step is taken by imposing electromagnetic wave.

1.1. Deformation step

In this step, we address the isotropic rubbery (amorphous) phase of SMPs. Above the glass transition temperature, SMPs exhibit the feature of an elastomer. The change in the internal energy is assumed to be negligible in the derivation of governing equations. First, the stress in the rubbery part of SMPs is expressed as

$$\mathbf{T} = -p\mathbf{I} + \mu_a \mathbf{B}_{k_a} \quad (1)$$

where p denotes the Lagrange multiplier due to the incompressibility constraints, μ_a represents the modulus of the rubbery phase, and \mathbf{B}_{k_a} is the left Cauchy stretch tensor. The deformation gradient \mathbf{F}_{k_a} and the left Cauchy stress tensor \mathbf{B}_{k_a} are expressed as

$$\mathbf{F}_{k_a} = \begin{pmatrix} \Lambda_a(t) & 0 & 0 \\ 0 & \frac{1}{\sqrt{\Lambda_a(t)}} & 0 \\ 0 & 0 & \frac{1}{\sqrt{\Lambda_a(t)}} \end{pmatrix} \quad (2)$$

$$\mathbf{B}_{k_a} = \mathbf{F}_{k_a} \mathbf{F}_{k_a}^T = \begin{pmatrix} \Lambda_a^2(t) & 0 & 0 \\ 0 & \frac{1}{\Lambda_a(t)} & 0 \\ 0 & 0 & \frac{1}{\Lambda_a(t)} \end{pmatrix} \quad (3)$$

where Λ is the stretch of the amorphous phase of SMPs. For uniaxial extension, $T_{22} = T_{33} = 0$ and then $p = \frac{\mu_a}{\Lambda_a}$. The substitution of p into equation (1) yields

$$T_{11} = \mu_a \left(\Lambda_a^2 - \frac{1}{\Lambda_a} \right) \quad (4)$$

1.2. Cooling step

The phase transition from rubbery (amorphous) phase to glassy phase is considered. It is presumed that the glassy phase is in the same stress state as the rubbery phase at such a transition. When SMPs are cooled below their glass transition temperature, the stress induced by the co-existing two different phases, rubbery and glassy parts is expressed as

$$\mathbf{T} = -p\mathbf{I} + \mu_a(1 - \alpha)\mathbf{B}_{k_a} + \mu_g\alpha\mathbf{B}_{k_g} \quad (5)$$

$$\mathbf{T} = -p\mathbf{I} + (1 - \alpha)\mathbf{T}_a + \int_0^t \mathbf{B}_{m(\tau)}(t) \frac{d\alpha}{d\tau} d\tau \quad (6)$$

$$\mathbf{T} = -p\mathbf{I} + (1 - \alpha)\mathbf{T}_a + \int_0^t f(\mathbf{F}_{m(\tau)}(t)) \frac{d\alpha}{d\tau} d\tau \quad (7)$$

where $\mathbf{F}_{m(t)}(t) = \mathbf{F}_{m(\tau)}(\tau)\mathbf{F}_{\theta(\tau)}^{-1}(t)$. Here, $\mathbf{F}_{m(\tau)}(t)$ is the mechanical part of the deformation gradient, $\mathbf{F}_{\theta(\tau)}^{-1}(t)$ the thermal part of the deformation gradient, and τ the time at which the glassy phase is generated. As $\mathbf{F}_{m(\tau)}(t)$ increases with a decrease in $\mathbf{F}_{\theta(\tau)}^{-1}(t)$. As a result, the total deformation gradient $\mathbf{F}_{m(\tau)}(\tau)$ is not changed. The deformation gradients are given by

$$\mathbf{F}_{m(\tau)}(t) = \begin{pmatrix} \Lambda_m(t) & 0 & 0 \\ 0 & \frac{1}{\sqrt{\Lambda_m(t)}} & 0 \\ 0 & 0 & \frac{1}{\sqrt{\Lambda_m(t)}} \end{pmatrix} \quad (8)$$

$$\mathbf{F}_{\theta(\tau)}(t) = \mathbf{B}\mathbf{I} \quad (9)$$

where $\mathbf{B} = 1 + \int \alpha(\theta(t) - \theta(\tau))$.

$$\mathbf{F}_{m(\tau)}(\tau) = \begin{pmatrix} \Lambda_g(\tau) & 0 & 0 \\ 0 & \frac{1}{\sqrt{\Lambda_g(\tau)}} & 0 \\ 0 & 0 & \frac{1}{\sqrt{\Lambda_g(\tau)}} \end{pmatrix} \quad (10)$$

$$\mathbf{F}_{m(\tau)}(t) = \begin{pmatrix} \frac{\Lambda_g(t)}{\mathbf{B}} & 0 & 0 \\ 0 & \frac{1}{\mathbf{B}\sqrt{\Lambda_g(t)}} & 0 \\ 0 & 0 & \frac{1}{\mathbf{B}\sqrt{\Lambda_g(t)}} \end{pmatrix} \quad (11)$$

Then,

$$\mathbf{B}_{m(\tau)}(t) = \mathbf{F}_{m(\tau)}(t)\mathbf{F}_{m(\tau)}^T(t) = \begin{pmatrix} \frac{\Lambda_g^2(\tau)}{\mathbf{B}^2(t)} & 0 & 0 \\ 0 & \frac{1}{\mathbf{B}^2\Lambda_g(\tau)} & 0 \\ 0 & 0 & \frac{1}{\mathbf{B}^2\Lambda_g(\tau)} \end{pmatrix} \quad (12)$$

$$\mathbf{T} = (1 - \alpha) \left(\Lambda_a^2(t) - \frac{1}{\Lambda_a(t)} \right) + \frac{\mu_g}{\mu_a} \int_0^t \left(\frac{\Lambda_g^2(\tau)}{\mathbf{B}^2} - \frac{1}{\mathbf{B}^2(t)\Lambda_g(\tau)} \right) \frac{d\alpha}{d\tau} d\tau \quad (13)$$

where Λ_a denotes the stretch of the amorphous (rubbery) phase, Λ_g the stretch of the glassy phase, α the amount of glassy phase and $\frac{d\alpha}{d\tau}$ the phase transition rate.

1.3. Unloading step

In this step, the stress is unloaded. The stress is written as

$$T = -pI + \mu_a(1 - \alpha)B_{k_a} + \mu_g\alpha B_{k_g} \quad (14)$$

$$T = (1 - \alpha) \left(\Lambda_a^2 - \frac{1}{\Lambda_a} \right) + \frac{\mu_g}{\mu_a} \int_0^t B_{n(\tau)}(t) dt \quad (15)$$

$$T = (1 - \alpha) \left(\Lambda_a^2 - \frac{1}{\Lambda_a} \right) + \frac{\mu_g}{\mu_a} \int_0^t f(F_{n(\tau)}(t)) dt \quad (16)$$

The resulting deformation gradient is

$$F_{n(\tau)}(t) = F_{\text{unload}}(t)F_{m(\tau)}(t) \quad (17)$$

$$F_{n(\tau)}(t) = \begin{pmatrix} \Lambda(t) & 0 & 0 \\ 0 & \frac{1}{\sqrt{\Lambda(t)}} & 0 \\ 0 & 0 & \frac{1}{\sqrt{\Lambda(t)}} \end{pmatrix} \begin{pmatrix} \frac{\Lambda_g(\tau)}{B} & 0 & 0 \\ 0 & \frac{1}{B\sqrt{\Lambda_g(\tau)}} & 0 \\ 0 & 0 & \frac{1}{B\sqrt{\Lambda_g(\tau)}} \end{pmatrix} \quad (18)$$

$$T = (1 - \alpha) \left(\Lambda_a^2(t) - \frac{1}{\Lambda_a(t)} \right) + \frac{1}{B^2} \frac{\mu_g}{\mu_a} \int_0^t \left(\Lambda(t)\Lambda_g^2(\tau) - \frac{1}{\Lambda(t)\Lambda_g(\tau)} \right) \frac{d\alpha}{d\tau} d\tau \quad (19)$$

1.4. Recovery step

As SMPs are heated by the microwave irradiation, the phase transition from glass phase to rubbery phase occurs. Provided that the stress of SMPs is zero during heating, the following equation can be obtained.

$$(1 - \alpha) \left(\Lambda_a^2(t) - \frac{1}{\Lambda_a(t)} \right) + \frac{\mu_g}{\mu_a} \int_0^t \left(\frac{\Lambda_g^2(\tau)}{B^2} - \frac{1}{B^2(t)\Lambda_g(\tau)} \right) \frac{d\alpha}{d\tau} d\tau = 0 \quad (20)$$

This equation is re-expressed as

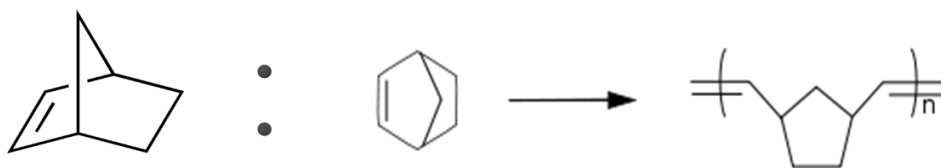
$$(1 - \alpha)\Lambda_a^3 + x\Lambda_a - (1 + \alpha) = 0 \quad (21)$$

where $x = -\frac{\mu_g}{\mu_a} \int_0^t \left(\frac{\Lambda_m^2(\tau)}{B^2} - \frac{1}{B^2(t)\Lambda_m(\tau)} \right) \frac{d\alpha}{d\tau} d\tau = 0$

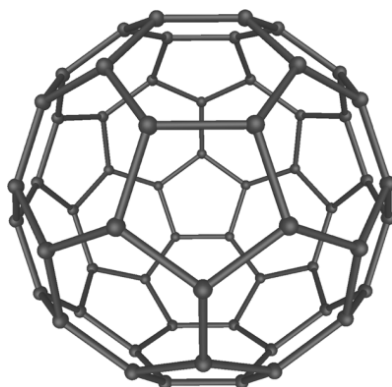
2. Materials

The Polynorbornene used in this study is described in Fig. S2 a. Fullerene is a carbon material that has a form of sphere in general. The spherical fullerene called a buckyball consists of pentagonal and hexagonal rings (Fig. S2 b)³⁵. Fullerenes are insoluble in water but soluble in organic solvents such as toluene and xylene. Depending on solvents, the C₆₀ solution has different color (Fig. S2 c). This is because the intermolecular interaction induces the overlap and broadening of the energy bands of fullerenes.

(a)



(b)



(c)

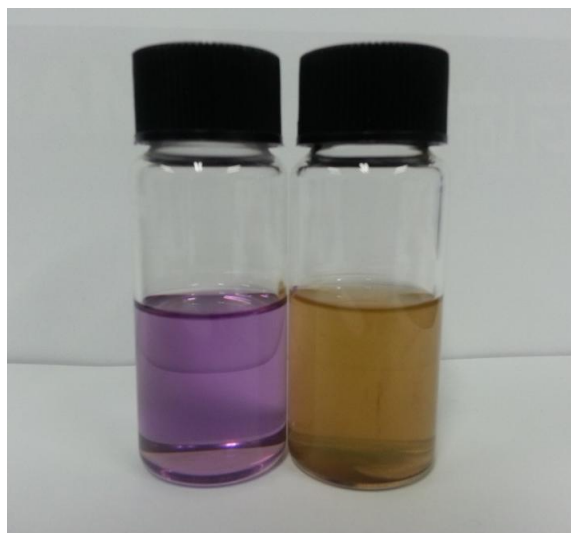


Fig. S2. Materials and solution of fullerenes. **a**, Molecular structure of Polynorbornene. **b**, Structure of C_{60} fullerene. The fullerene has the buckyball structure with pentagonal and hexagonal rings. **c**, Fullerene solution. The images indicate the fullerene solutions in toluene (right hand side) and acetone (left hand side).

3. Preparation methods

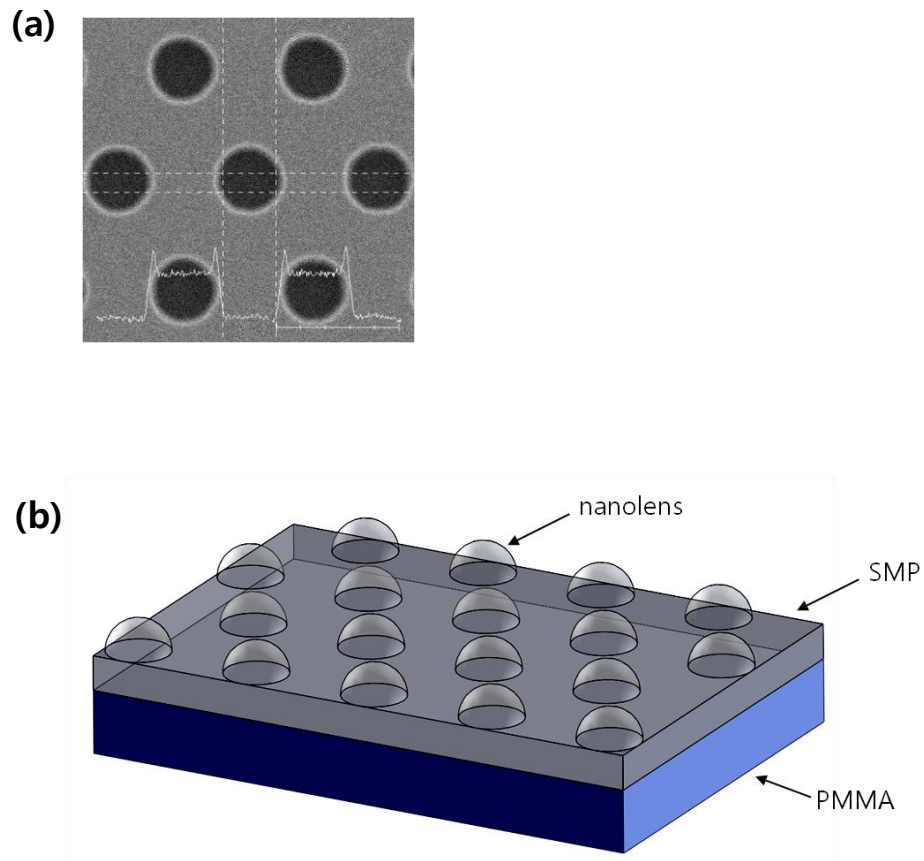


Fig. S3. Master mold and fullerene embedded nanolens array. **a**, SEM image of the master mold employed in this study. The mold has the hexagonal arrangement of nanolenses. **b**, Schematic image of the fullerene embedded nanolens array.

4. Morphological analysis

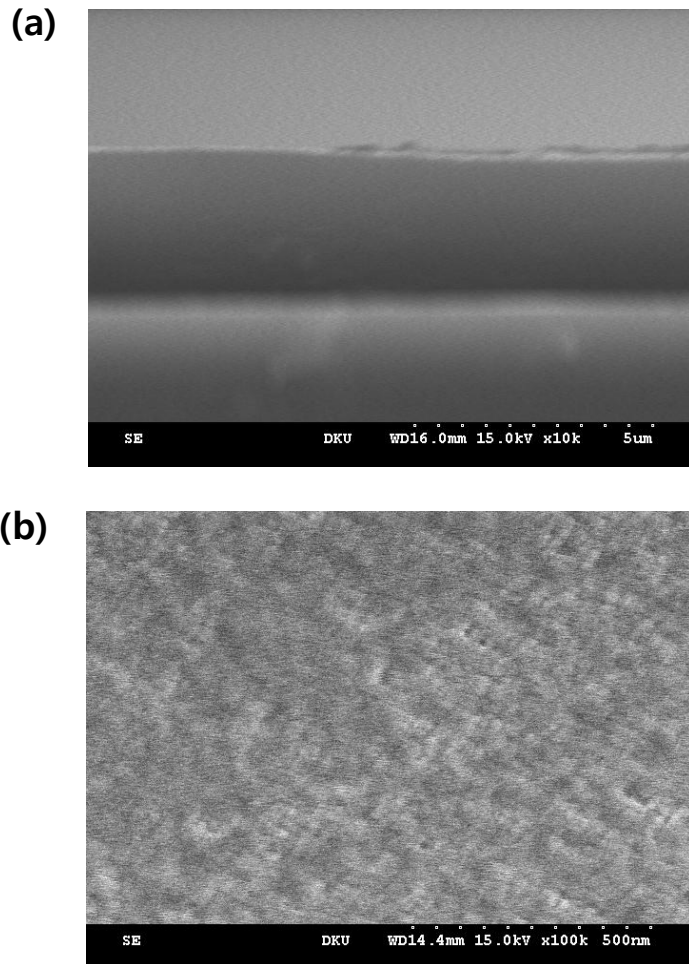


Fig. S4. SEM analysis. **a**, SEM image of the cross-sectional area of the nanolens array. **b**, SEM image of the top surface of the nanolens array.

For the SEM observation, Pt was coated on top of the samples for 2 min. Its thickness was 6 nm.

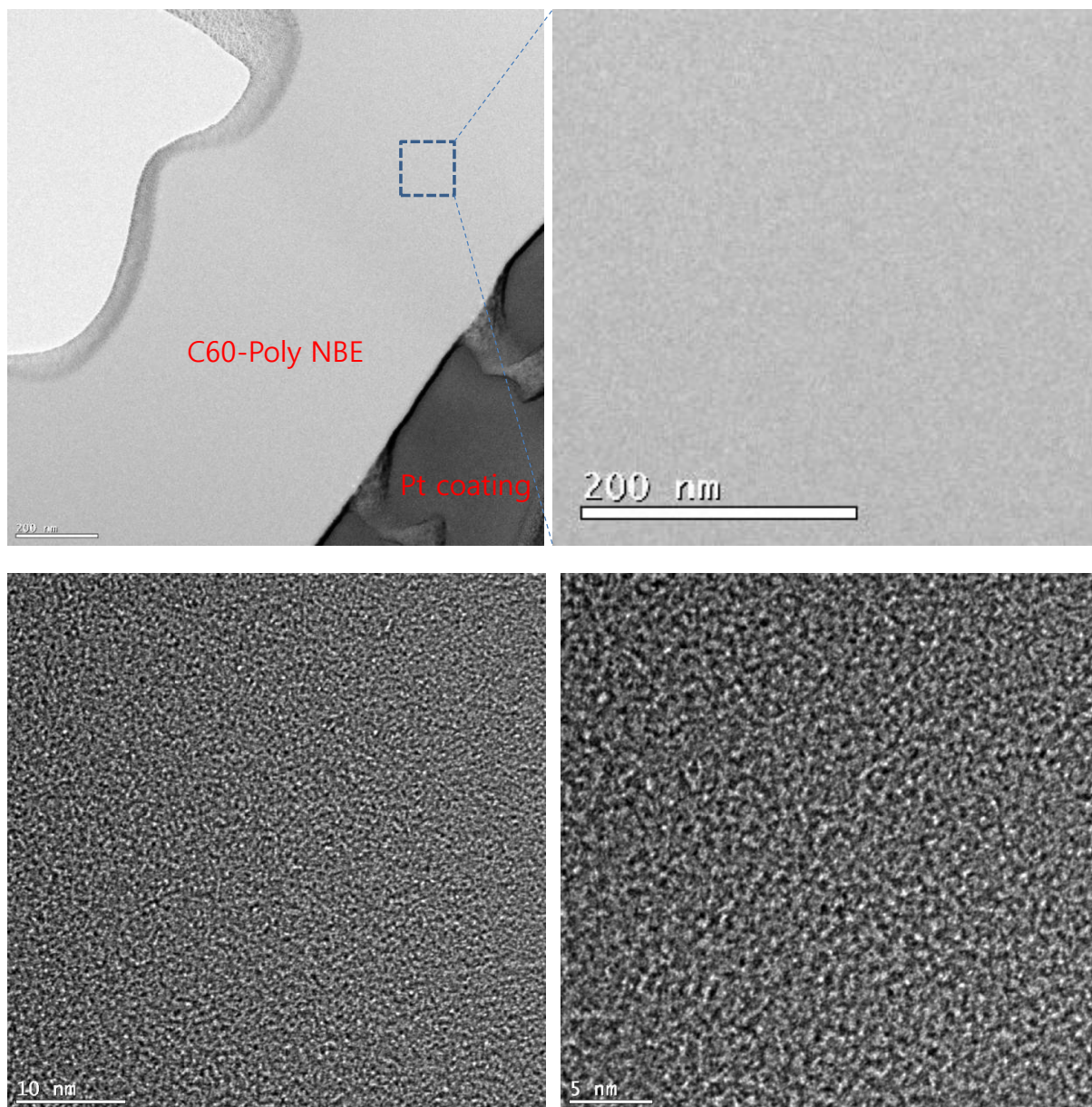


Fig. S5. TEM analysis. We observed the TEM images of the cross-sectional area of the nanolens array at different magnifications.

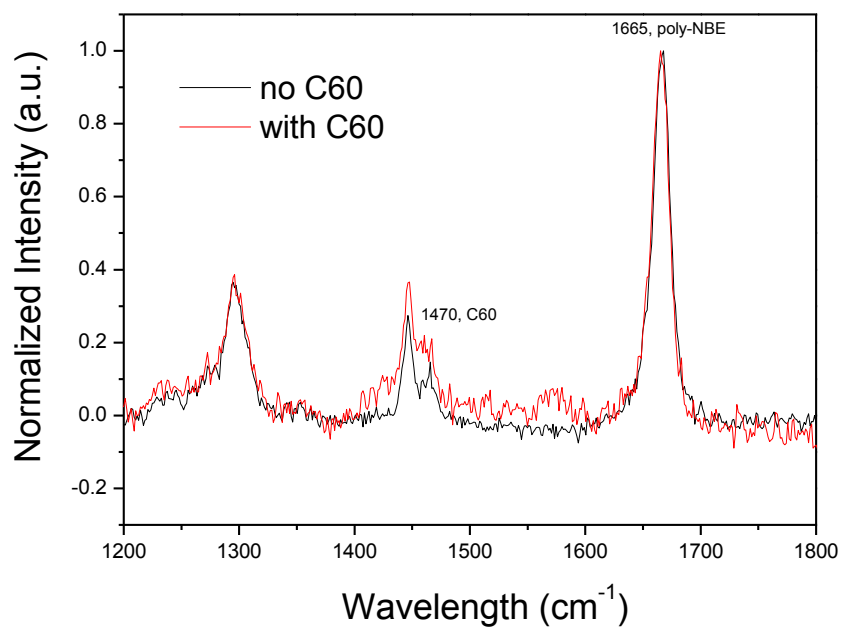


Fig. S6. Raman spectroscopy analysis. We observed the characteristic peak of C60 at 1470 cm⁻¹.

5. Optical analysis

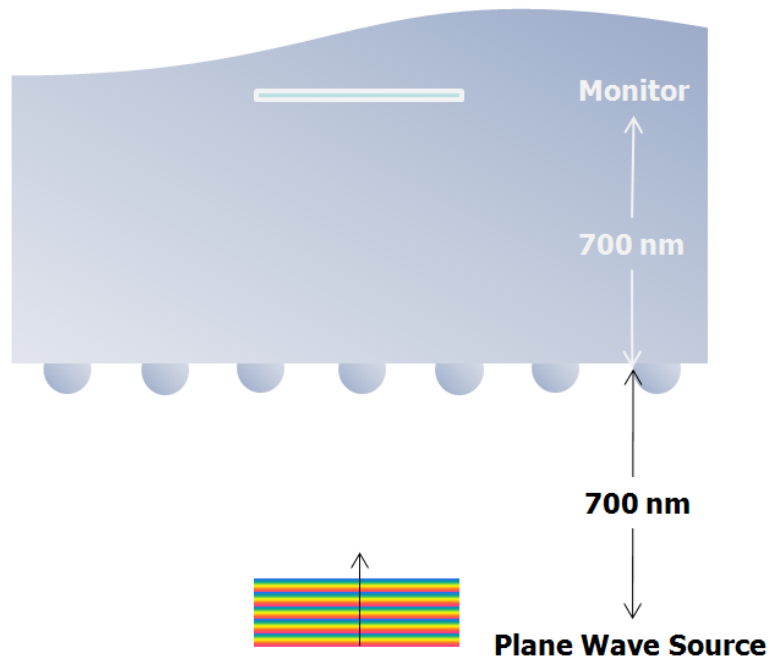


Fig. S7. Schematic illustration of optical calculation. The plane wave source is used in the FDTD method, and the resulting transmittance is monitored at a position apart from the nanolens surface by 700 nm.

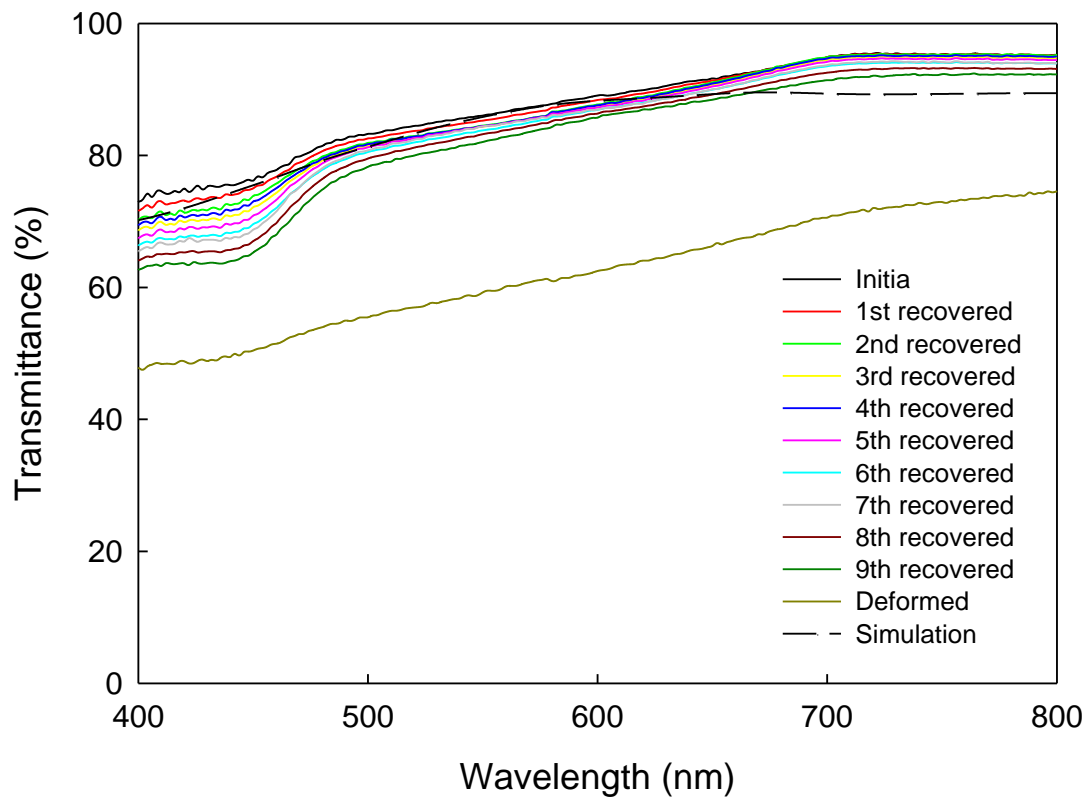


Fig. S8. Optical characterization for repeatability. The transmittance measurements are repeated to evaluate the optical repeatability of the nanolens array. This finding indicates that the nanostructure shows considerable sustainability during the repeatability test.

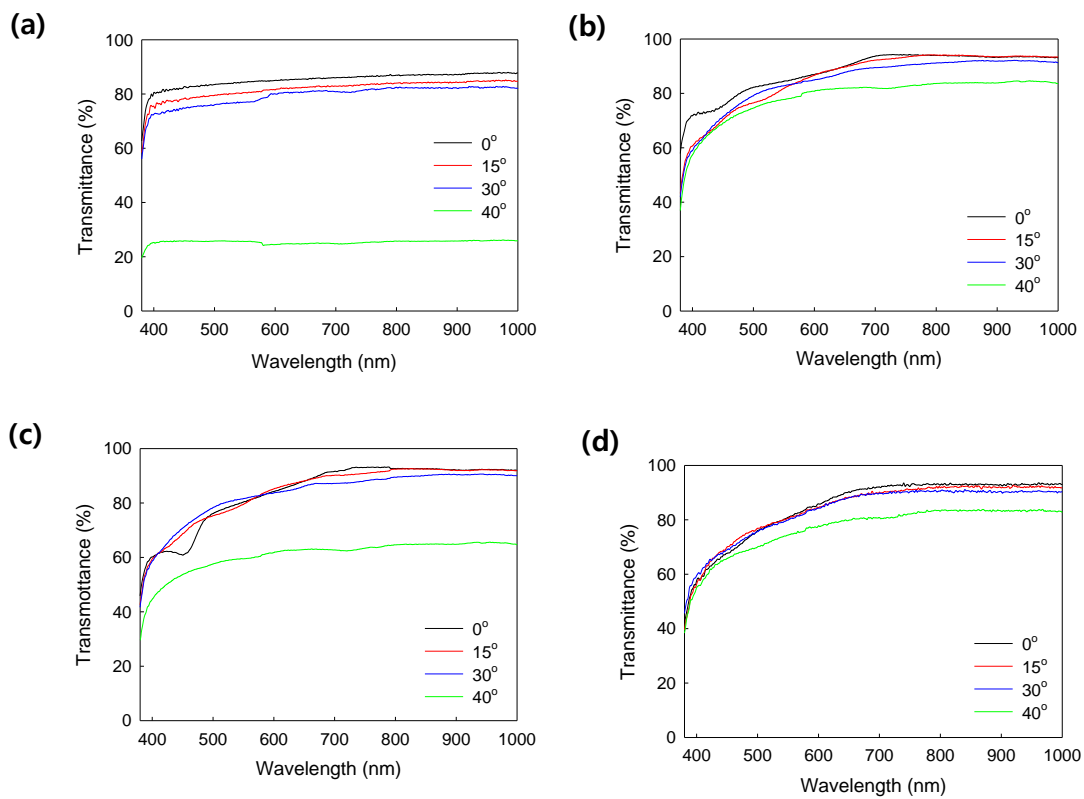


Fig. S9. Effect of the incident light angle. **a**, Transmittance for a flat plane of pure Polynorbornene with respect to wavelength. The transmittance measurements are carried out at the different angles of incident light (0°, 15°, 30°, and 40°). The sharp decrease in the light transmittance is observed at the 40° angle. **b**, Transmittance of the nanolens array without fullerenes. The transmittance at the 40° angle is not decreased sharply due to the nanolens structure. **c**, Transmittance of the nanolens array without fullerenes when the incident light enters from the back side of the nanolens array structure. **d**, Transmittance of the fullerene embedded nanolens array. The similar result to that shown in (b) is observed.

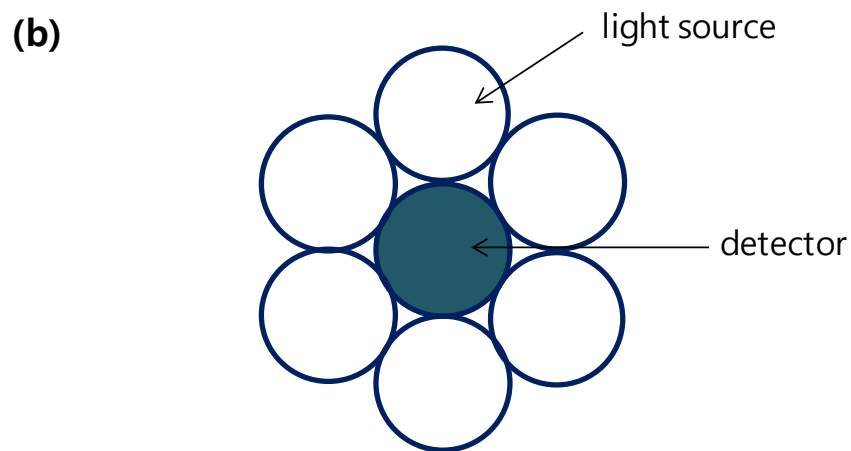
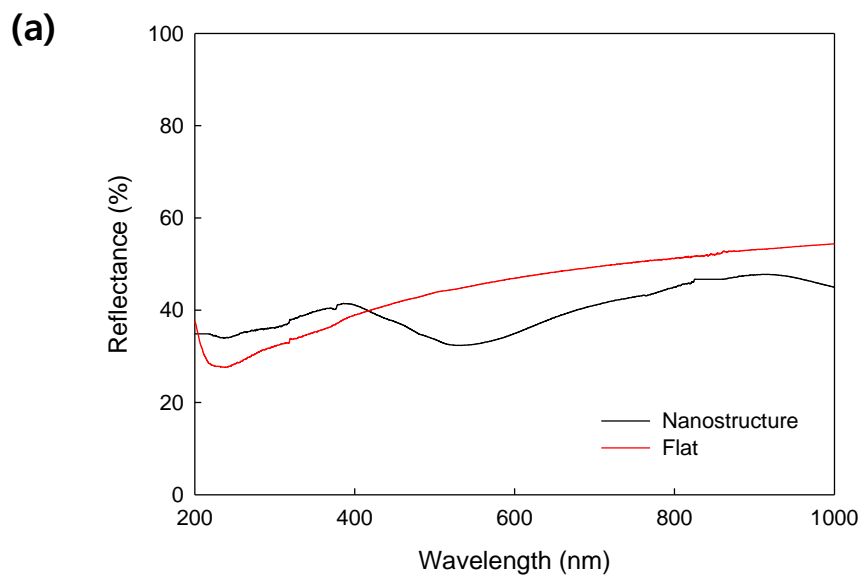


Fig. S10. Reflectance characterization. **a**, Reflectance as a function wavelength. The reflectance result of the nanolens array is compared with that of a flat plane. **b**, Schematic diagram of the reflection fiber optic probe used for the LSPR experiment.

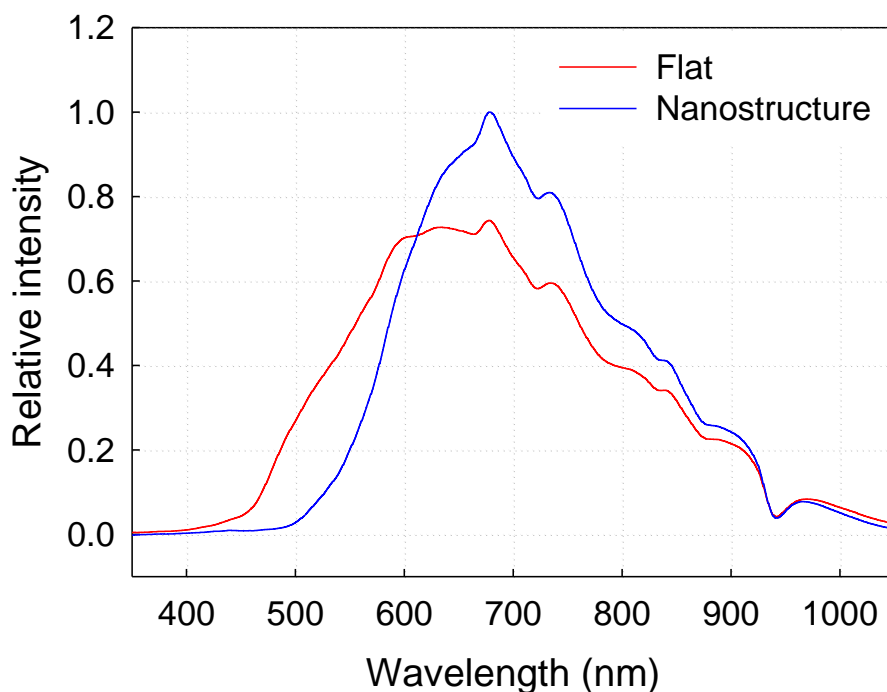


Fig. S11. Localized surface plasmon resonance (LSPR). The enhanced resonance intensity is observed in the nanolens array.

The localized surface plasmon resonance (LSPR), a resonance phenomenon of free electron wave in metal nanostructures and particles, can characterize the nanolens array. Compared with a flat surface, the enhanced resonance intensity is observed in the nanolens array due to the formation of the so-called hot-spot effect induced by the nanostructure (Fig. S11).

The LSPR measurement was performed using a reflection fiber optic probe (Oceanoptics, R 400) after coating Pt on the surface of nanolens array (Supplementary Fig. S8b). A white light (ANDO, AQ-4303B) and optical fibers (multimode, 105 μm /125 μm) were used for the experiments.

6. Mechanical analysis

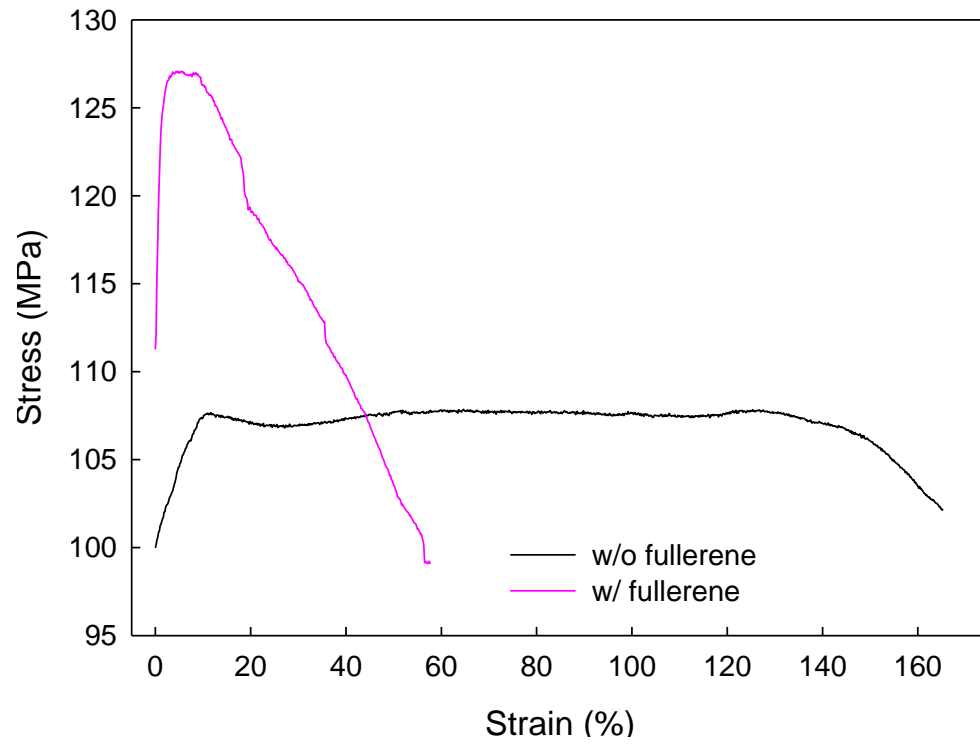


Fig. S12. Tensile test. Stress-strain curves of specimens with fullerenes and without fullerenes. The addition of fullerenes leads to remarkably different mechanical behavior.

Table. S1. Tensile test. Characterization of mechanical properties of fullerene incorporated SMPs compared with SMPs without fullerenes. Significant improvement of mechanical properties for fullerene reinforced SMPs was detected from the nanoindentation experiment and the tensile test. Young's modulus of the SMPs filled with fullerenes is significantly increased. This implies that fullerenes can be used as a good reinforcing agent.

Property	w/ fullerene	w/o fullerene
Tensile Strength (MPa)	128	108
Young's modulus (MPa)	1290	124
Hardness (MPa)	151	108
Elongation at break (%)	58	165

The thermomechanical tests were carried out using a universal testing machine equipped with a temperature-controlled chamber. The dimensions of the specimens were 60 mm in length, 10 mm in width, and 0.05 mm in thickness. A load cell of 2.5 kN was used and the gauge length was 25 mm. The specimen was extended to 50 % strain at a speed of 10 mm/min at 20 °C above T_g and then quenched to the fixing temperature, 20 °C below T_g for 20 min. Afterwards, the specimen was heated at the recovery temperature, 20 °C above T_g for 10 min. The tests were repeated three times. The important quantities to characterize the shape memory properties are the strain recovery rate (R_r) and strain fixity rate (R_f) expressed as below:

$$R_r = \frac{\varepsilon_m - \varepsilon_p(N)}{\varepsilon_m - \varepsilon_p(N-1)} \times 100 \quad (22)$$

$$R_f = \frac{\varepsilon_u(N)}{\varepsilon_m} \times 100 \quad (23)$$

where ε_m is the maximum strain in the test, ε_p indicates the residual strain after unloading, N means the number of cycle in the test, and ε_p denotes the residual strain after recovery (see Fig. S1). The strain recovery rate characterizes the ability of an SMP to memorize its permanent shape, while the strain fixity rate quantifies the ability of an SMP to fix the strain given to the sample. The strain recovery rate and fixity rate measured for the fullerene embedded specimens are listed in the following table.

	1 st cycle	2 nd cycle	3 rd cycle
Strain recovery rate (%)	84	82	80
Strain fixity rate (%)	85	86	88

On the other hand, it is not easy to measure such quantities for nanopatterns fabricated using SMPs. Thus, we proposed a new quantity, shape recovery ratio (R_s) for characterizing the shape recovery effect of nanopatterns.

$$R_s = \frac{H_i}{H_r} \times 100 \quad (24)$$

Where H_i is the initial length (or height) of nanostructures and H_r is the length of nanostructures after recovery.

7. Contact angle analysis

Thermodynamic analysis is performed to understand the contact angle behavior of the nanolens array. For the noncomposite state, the corresponding geometrical relation and free energy differences are expressed as follows:

$$\theta_i \frac{L_i^2}{\sin^2 \theta_i} - L_i^2 \cot \theta_i - \alpha r^2 + r^2 \sin \alpha \cos \alpha = \theta_j \frac{L_j^2}{\sin^2 \theta_j} - L_j^2 \cot \theta_j \quad (25)$$

$$F_{i \rightarrow j} / \gamma = \left(\theta_j \frac{L_j}{\sin \theta_j} - \theta_i \frac{L_i}{\sin \theta_i} \right) + 2r\alpha \cos \theta_Y \quad (26)$$

$$\theta_i \frac{L_i^2}{\sin^2 \theta_i} - L_i^2 \cot \theta_i = \theta_k \frac{L_k^2}{\sin^2 \theta_k} - L_k^2 \cot \theta_k - (a + 2r)r \cos \alpha + r^2 \left(\frac{\pi}{2} - \alpha \right) + r^2 \sin \alpha \cos \alpha \quad (27)$$

$$F_{i \rightarrow k} / \gamma = \left(\theta_k \frac{L_k}{\sin \theta_k} - \theta_i \frac{L_i}{\sin \theta_i} \right) + \left\{ a + 2r \left(\frac{\pi}{2} - \alpha \right) \right\} \cos \theta_Y \quad (28)$$

where γ is the liquid surface tension, F is the FE, and θ_Y is the intrinsic CA. Those equations are calculated repeatedly to obtain the equilibrated contact angles of the Wenzel and Cassie states.

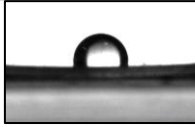
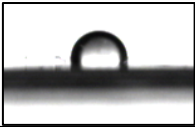
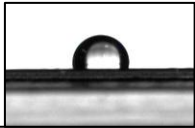
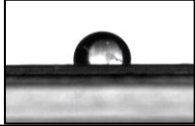
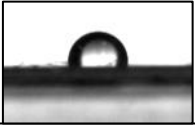




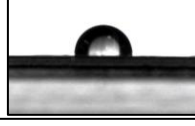
Test no.	Contact angle (°)	Image
1	113	
2	112	
3	112	
4	110	
5	109	
6	109	
7	108	
8	108	
9	108	
10	106	

Fig. S13. Contact angle characterization for repeatability. The contact angle measurements are repeated to evaluate the repeatability of the nanolens array. Similar to the optical repeatability, the nanostructure shows good sustainability.

8. Supplementary references

31. Srivastava V, Chester SA, Anand L. Thermally actuated shape-memory polymers: Experiments, theory, and numerical simulations. *Journal of the Mechanics and Physics of Solids* 2010, **58**: 1100-1124.
32. Liu Y, Gall K, Dunn MI, McCluskey P. Thermomechanics of shape memory polymer nanocomposites. *Mechanics of Materials* 2004, **36**: 929-940.
33. Baghani M, Naghdabadi R, Arghavani J. A large deformation framework for shape memory polymers: Constitutive modeling and finite element implementation. *Journal of Intelligent Material Systems and Structures* 2013, **24**: 21-32.
34. Barot G, Rao IJ. Constitutive modeling of the mechanics associated with crystallizable shape memory polymers. *Zeitschrift für angewandte Mathematik und Physik* 2006, **57**: 652-681.
35. Fullerene. *Encyclopædia Britannica on-line*.